

1           **Unraveling the role of feed temperature and cross-flow velocity on organic fouling in**  
2                           **membrane distillation using response surface methodology**

3

4 Francesco Ricceri<sup>a</sup>, Bastiaan Blankert<sup>b</sup>, Johannes S. Vrouwenvelder<sup>b</sup>, Alberto Tiraferri<sup>a\*</sup>, Luca  
5 Fortunato<sup>b\*</sup>

6

7 <sup>a</sup> Department of Environment, Land and Infrastructure Engineering (DIATI), Politecnico di Torino,  
8 Corso Duca degli Abruzzi 24, Turin, 10129, Italy

9 <sup>b</sup> Water Desalination and Reuse Center (WDRC), King Abdullah University of Science and  
10 Technology (KAUST), Biological & Environmental Science & Engineering Division (BESE),  
11 Thuwal 23955-6900, Saudi Arabia

12

13 \* Corresponding authors

14 **Highlights**

- 15 • Feed temperature governs the fouling behaviour more than cross-flow velocity
- 16 • Higher feed temperature increases the fouling accumulation
- 17 • Higher cross-flow velocity decreases the fouling accumulation
- 18 • Feed temperature and cross-flow velocity were statistically significant for the RSM
- 19 • RSM is a powerful tool to assess performance and fouling behaviour in MD

20 **Abstract**

21 Understanding the role of operating condition on fouling development in membrane distillation  
22 (MD) is critical for the further optimization of MD technology. In this study, organic fouling  
23 development in MD was investigated with a synthetic model solution of humic acid varying the  
24 feed inlet temperature from 35 to 65 °C and the cross-flow velocity from 0.21 to 0.42 m/s. For  
25 each experiment, the final fouling layer thickness was estimated using optical coherence  
26 tomography, a non-invasive imaging technique. The set of experiments was mined to model the  
27 initial flux decline, the final flux, and the final foulant thickness responses by central composite  
28 design, a useful response surface methodology (RSM) tool. A strong influence on the initial flux  
29 was observed by varying feed inlet temperature. The results indicated a linear increment of the  
30 fouling thickness by increasing the feed inlet temperatures. Overall, the feed inlet temperature  
31 governed both the initial flux decline and the fouling deposition rate. A more complex behaviour  
32 was observed by varying the cross-flow velocity. To this extent, higher cross-flow velocities  
33 showed a positive effect on the initial flux, which however translated in larger values of the  
34 initial flux decline rate. On the other hand, the higher shear stress contributed to a decrease of the  
35 final fouling layer thickness. The proposed approach was proven to be a valuable tool to assess  
36 the role of the operating conditions on fouling and process performance in MD.

37

38 **Keywords:** Direct contact membrane distillation (DCMD); Membrane fouling; Optical  
39 coherence tomography (OCT); Response surface methodology (RSM);

## 40 **1 Introduction**

41 Membrane distillation is a thermal-based desalination technology which has gained an  
42 exponential interest during the last decades [1, 2]. Among all the possible membrane distillation  
43 configurations, direct contact membrane distillation (DCMD) is the most compact. Due to its  
44 simplicity, this process has been extensively studied at laboratory scale to approach scale-up  
45 applications in MD [3-5]. In fact, DCMD does not require an external condenser and it is more  
46 suitable for water-based applications than air gap, vacuum, or sweep gas membrane distillation.  
47 In DCMD, the hot feed and the cold permeate solutions are in contact with a hydrophobic  
48 membrane. Under ideal working conditions, only water vapor passage is allowed through this  
49 microporous membrane [6, 7]. However, several operational challenges might cause decrease in  
50 productivity or even process failure [8]. According to the type of treated feed solution, three  
51 main drawbacks observed in the operational DCMD phase are: (i) pore wetting, (ii) mineral  
52 scaling, and (iii) membrane fouling. Wetting mainly occurs when membrane hydrophobicity is  
53 reduced, together with the liquid entry pressure, to the point which allows liquid passage through  
54 the pores [9, 10]. Wetting is easily induced by amphiphilic molecules, such as surfactants, and it  
55 leads to process failure even in a preliminary recovery stage [11, 12]. Mineral scaling is due to  
56 crystal formation of salts at the solid membrane interface, initiating a rapid and severe flux  
57 decline which can also translate into pore wetting and membrane damage [13]. Membrane  
58 fouling leads to flux reduction over time due by accumulation of feed contaminants on the  
59 membrane surface [14].

60 With the increasing interest in MD, the number of possible applications has been also expanded.  
61 As a thermal-based process, MD has been largely used for desalination to produce high-quality  
62 water while concentrating the feed above typical reverse osmosis limits [15]. Recently, DCMD

63 has been also employed for the treatment of challenging wastewater, such as produced water,  
64 textile, and pharmaceutical wastewater [16-18]. Within this range of possible applications, recent  
65 studies demonstrated how effective pre-treatment strategies and process optimization could  
66 highly reduce pore-wetting and mineral scaling propensity [16, 19]. In this context, membrane  
67 fouling is still considered one of the main bottlenecks of MD operations [20, 21]. Among  
68 different foulant species, humic substances showed particularly high fouling propensity in low-  
69 pressure processes due to high adhesion capacity of these compounds on the membranes [22].  
70 Humic acids are also the major constituents of natural organic matter, as well as widely present  
71 constituents in surface water, groundwater, and seawater [23]. In this study, organic fouling in  
72 DCMD was investigated by using humic acid as model compound under accelerated fouling  
73 conditions.

74 Optical coherence tomography (OCT) has been recently demonstrated as an effective and  
75 versatile tool for fouling characterization. This non-destructive technique enables monitoring the  
76 filtration system under continuous operation, providing real-time information of the fouling layer  
77 [24, 25]. OCT allows acquiring non-invasively 2D cross-sectional and 3D volumetric images  
78 with micron-level resolution without interfering with the membrane operation. Recently, the use  
79 of OCT has been employed for studying the fouling behavior in MD when treating textile,  
80 pharmaceutical wastewater, and concentrated brines [17, 18, 26]. In these studies, OCT results  
81 were efficiently linked to process performance data allowing an in-depth understanding on how  
82 fouling and scaling impact the water flux during the DCMD process. However, these literature  
83 studies were often limited to narrow ranges of operative conditions in MD. To extend the  
84 understanding of fouling under a wider range of temperatures and cross-flow velocities, response  
85 surface modeling (RSM) was implemented in this study through Design Expert software [27-29].

86 One of the way to implement RSM is by using central composite design (CCD), an array  
87 whereby investigated parameters are efficiently distributed to allow a second-order generalized  
88 regression between the experimental results [30, 31]. Recently, RSM combined with CCD has  
89 gained a growing interest in membrane process optimization as it is able to consider several  
90 variables at the same time with easy evaluation of the generated responses. An interesting  
91 application of RSM in MD was developed by Shokrollahi et al., who effectively modeled flux  
92 and thermal efficiency for a wide range of interacting parameters [32]. There, numerical  
93 modeling with CCD method for flux optimization showed that temperature and module length  
94 have the most important influence on MD productivity.

95 In this study, central composite design is implemented to guide the design of MD experiments  
96 conducted with different combinations of feed inlet temperature and cross-flow velocity. The  
97 experiments are performed with a synthetic model solution of humic acid, where the distillate  
98 flux is monitored as a function feed volume concentration factor. Additionally, OCT *in-situ*  
99 monitoring is employed to characterize the fouling layer developed at the end of each MD test.  
100 The flux performance and fouling data are discussed and critically examined also to assess a  
101 valuable experimental based modeling. Therefore, (i) the initial flux decline rate, (ii) the final  
102 flux, (iii) the total flux decline, and (iv) the final fouling thickness are applied as responses  
103 (dependent variables) in the RSM analysis to investigate the mechanism of fouling and to  
104 identify the most suitable DCMD operating conditions. The investigation assesses the role of  
105 process parameters and governing factors on fouling in MD, and it proposes the rational  
106 deployment of RSM as a tool to move toward scale-up applications.

## 107 2 Materials and Methods

108

### 109 2.1 Membrane and Feed composition

110 Accelerated fouling conditions were employed in this study using a synthetic feed solution with  
111 an initial humic acid (HA) concentration of 500 mg/L in deionized (DI) water. To enhance the  
112 fouling deposition, 20 mM of calcium chloride, CaCl<sub>2</sub>, was also added to the feed solution [33].  
113 HA and CaCl<sub>2</sub> were purchased from Sigma-Aldrich. The organic compound was received in  
114 powder form. The stock solution was prepared by dissolving the chemicals in 600 mL of DI  
115 water. The stock was then added, prior to flux stabilization, to the remaining 400 mL of  
116 deionized water used as initial feed. Initial volumes of 1 L were thus used for both the feed and  
117 permeate solutions, the latter consisting of DI water.

118 A commercially available hydrophobic polytetrafluoroethylene with a polypropylene support  
119 (PP-PTFE) membrane (Membrane Solutions corp., US) was used for all the experiments. The  
120 membrane characteristics, provided by the manufacturer or obtained in the lab, are listed in Table  
121 1. The membrane permeability coefficient was calculated by dividing the experimental water  
122 flux by the vapor pressure difference across the membrane (see calculated angular coefficient  
123 from Fig S.1).

124 **Table 1.** Porous PP-PTFE membrane characteristics

Data source	Parameter	Units	Value
Provided by the manufacturer	Thickness	µm	174 - 245
	Mean pore size	µm	0.22
	Bubble point	psi	16.0-20.3
From experiments	Membrane permeability coefficient	kg m <sup>-2</sup> h <sup>-1</sup> bar <sup>-1</sup>	143.8

125

## 126 2.2 MD lab setups

127 All the MD tests were performed in direct contact membrane distillation (DCMD) configuration  
128 with a lab-scale batch system. In this process, the feed and permeate streams were circulated  
129 counter-currently on their respective sides of the hydrophobic membrane, not enabling liquid  
130 passage through the pores. Thanks to the applied thermal gradient, the colder liquid is enriched  
131 by the water vapor extracted from the feed stream during the process. Ranges of feed  
132 temperature of 35 - 65 °C and feed cross-flow velocity of 0.21 - 0.42 m/s (deriving from a cross-  
133 flow rate ranging from 25 to 50 L/h) were investigated in this study. To clearly assess the role of  
134 feed parameters on fouling deposition, a constant temperature and cross-flow velocity of 20 °C  
135 and 0.1 m/s were maintained in the permeate side. For the same reason, no feed spacer was used.  
136 The temperatures in the feed and permeate inlet of the flow cell were maintained constant  
137 throughout the experiment using a thermostatic water bath and a chiller (Corio-CD, Julabo,  
138 Germany). The heat exchangers were accurately controlled by the temperature sensors integrated  
139 in the conductivity meters (TetraCon 325, Xylem Analytics, Germany) located just before the  
140 inlet of the flow cell. On the permeate side, purified water with electrical conductivity below 20  
141  $\mu\text{S}/\text{cm}$  was used, whereas the initial feed conductivity was  $4.2 \pm 0.2 \text{ mS}/\text{cm}$ . For each  
142 experiment, the permeate conductivity was continuously monitored to ensure no liquid passage  
143 during the tests, i.e., no pore wetting. Cross-flow velocity and outlet-temperature were measured  
144 by digital cross-flow meters located in proximity of the flow cell outlet. The flux across the  
145 membrane was calculated by recording the change in weight of the permeate tank in time  
146 through a computer-interfaced balance. All the instruments were digitally connected and  
147 controlled by Lab View software. The DCMD flow cell in polymethyl methacrylate was

148 customized to allow *in-situ* characterization with OCT. The flow cell was had dimensions of 10.0  
149  $\times 3.3 \times 0.1$  cm (length  $\times$  width  $\times$  height) for a total active membrane area of 33 cm<sup>2</sup>.

### 150 **2.3 Design of experiments and statistical analysis**

151 Design Expert software was used to setup and analyze the response surface methodology (RSM)  
152 for DCMD experiments. Central composite design (CCD) was applied to define the number of  
153 runs needed for the optimization of the variables and responses. Feed inlet temperature and  
154 cross-flow velocity were selected as operating factors, while the initial flux decline rate, the final  
155 flux, and the final thickness of the fouling layer were selected as responses after a preliminary  
156 phase investigation of experimental results. The Supplementary Material appendix presents  
157 further details of the applied CCD method and analyses. The selected ranges of investigation for  
158 the various factors are reported in Table 2, together with the coded experimental values  
159 extrapolated by Design Expert software. The CCD method generated a suggestion for nine total  
160 runs, each with a specific combination of values of T<sub>f</sub> and CFV. This procedure allowed  
161 weighted probing of the entire multidimensional space. The experimental results were used as  
162 input data to generate the model for each response according to the best fit. ANOVA was used  
163 for the statistical analysis of the results to evaluate the quality of the model.

164 **Table 2.** Experimental design of the selected of operating conditions, representing the range of  
165 experimental variables used in the RSM model

Factors	Unit	Minimum	Maximum	Coded low	Coded high	Mean
Temperature	(C°)	35.0	65.0	40.0	60.6	50.0
Cross-flow velocity	(m/s)	0.21	0.42	0.24	0.39	0.31

## 166 **2.4 Filtration experiments protocol**

167 Fouling experiments consisted of two phases: (i) a stable flux phase and (ii) a fouling phase. The  
168 flux was first stabilized using DI water only as feed, without organic foulants ( $J_0$ ). This stage  
169 allowed achievement of the hydrodynamic equilibrium. The fouling phase then started at time  
170 zero, when the appropriate amount of organic foulant stock solution was added into the feed  
171 tank. This second phase was run until a volume concentration factor of 2.5 was reached, which  
172 was always associated with sufficient operational time to obtain a near stable flux and fouling  
173 layer thickness. The increment of  $\text{CaCl}_2$  concentration during experiments can be considered  
174 negligible for any possible effect in the reduction of the feed vapor tension value. For this reason,  
175 the flux decrement observed during the fouling tests can be predominantly attributed to foulant  
176 deposition.

## 177 **2.5 Optical coherence tomography (OCT) analysis**

178 A spectral-domain optical coherence tomography (SD-OCT) system Ganymede II from  
179 Thorlabs, GmbH (Germany) was used to assess the fouling deposition on the membrane surface  
180 under accelerated fouling conditions. The OCT was equipped with a scan lens (LSM 03BB). The  
181 OCT probe was positioned on top of middle point of the DCMD module to characterize the  
182 fouling layer thickness at the end of each experiment. 3D cross-sectional OCT scans ( $666 \text{ pixel} \times$   
183  $666 \text{ pixel} \times 1022 \text{ pixel}$ ) corresponded to  $4.0 \text{ mm} \times 4.0 \text{ mm} \times 2.25 \text{ mm}$  (width  $\times$  length  $\times$  depth).  
184 The OCT scans were processed with the FiJi software. Images were filtered to reduce the noise,  
185 then the contrast and brightness were adjusted. 3D scans were then visualized by AVIZO (Field  
186 Electron and Ion Company, Hillsboro, OR, USA) software and modified for visualization  
187 purpose. The fouling layer thickness was calculated using a customized MATLAB code.

## 188 **3 Results and discussion**

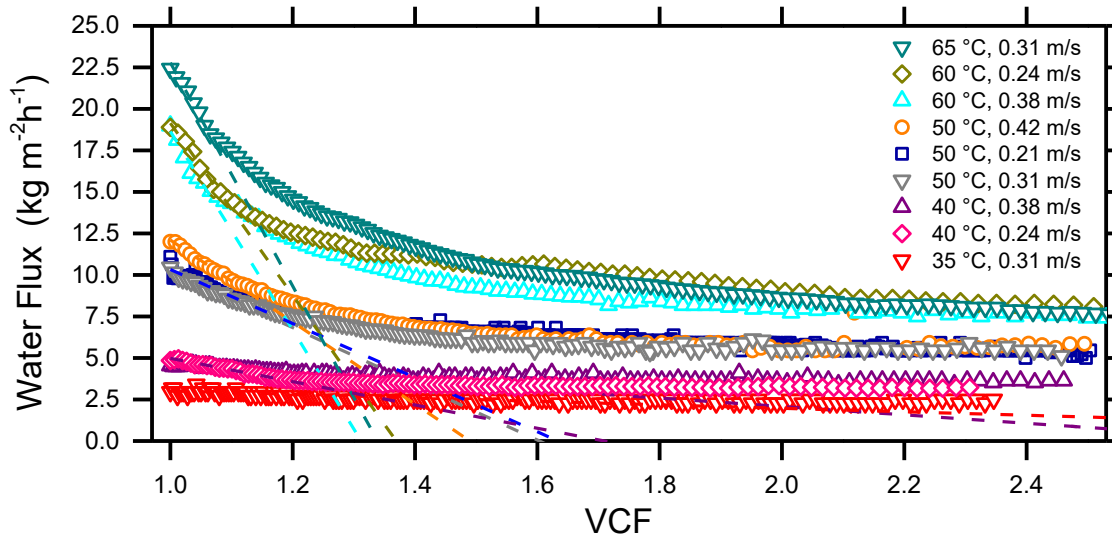
189

### 190 **3.1 Beyond the RSM: An overall picture of the process parameters in MD organic fouling**

#### 191 **3.1.1 The Effect of temperature and cross-flow velocity on the experimental flux**

192 This section describes the experimental results while providing an in-depth understanding of the  
193 selected responses (dependent variables) of the RSM model. In this study, Design Expert was  
194 employed as a statistical tool to create the experiment plan aimed at studying the impact of  
195 operating condition on the fouling behavior in DCMD. The list of experiments is reported in  
196 Table S.1 and in the legend of Fig 1, where experimental results of water production in DCMD  
197 at different operating conditions are also shown.

198 In DCMD process, the initial flux,  $J_0$ , is related to the feed temperature and cross-flow velocity  
199 [34, 35]. As expected, in this study the inlet feed temperature was found to govern  $J_0$ . By  
200 increasing  $T_f$  from 35 to 65 °C, the  $J_0$  increased from 3 to 22.5 kg m<sup>-2</sup>h<sup>-1</sup>, while increasing the  
201 cross-flow velocity from 0.21 to 0.42 m/s at fixed  $T_f$  50 °C led to an increase of only 2 kg  
202 m<sup>-2</sup>h<sup>-1</sup>. This result can be attributed to the nature of the driving force, namely, the vapor tension  
203 difference between the feed and the permeate, which can be easily determined through Antoine  
204 equation [36]. On the other hand, the cross-flow velocity can contribute to the flux increment by  
205 reducing the temperature polarization effects [37].



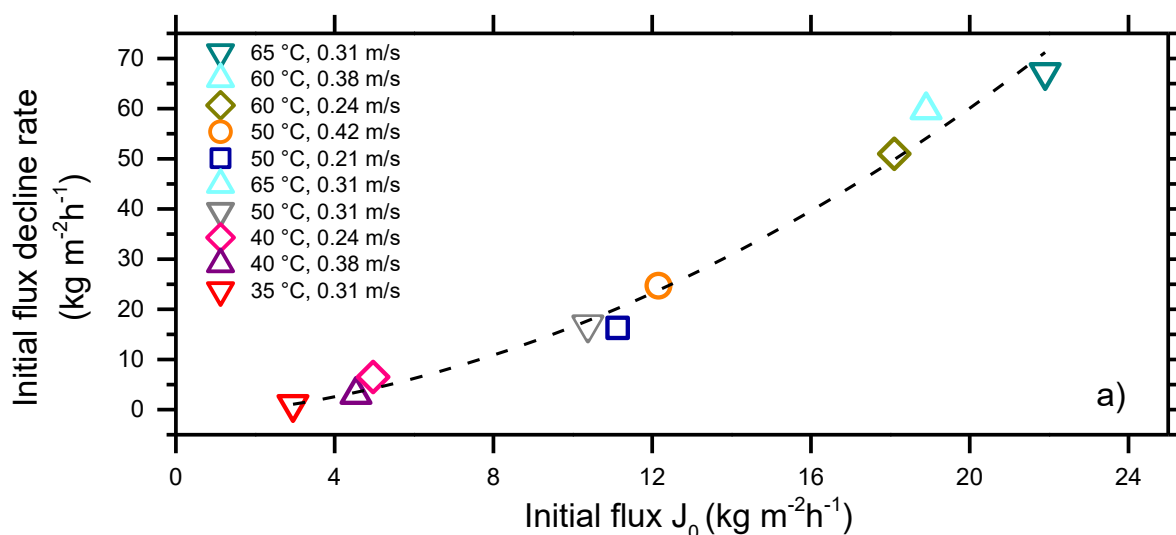
206

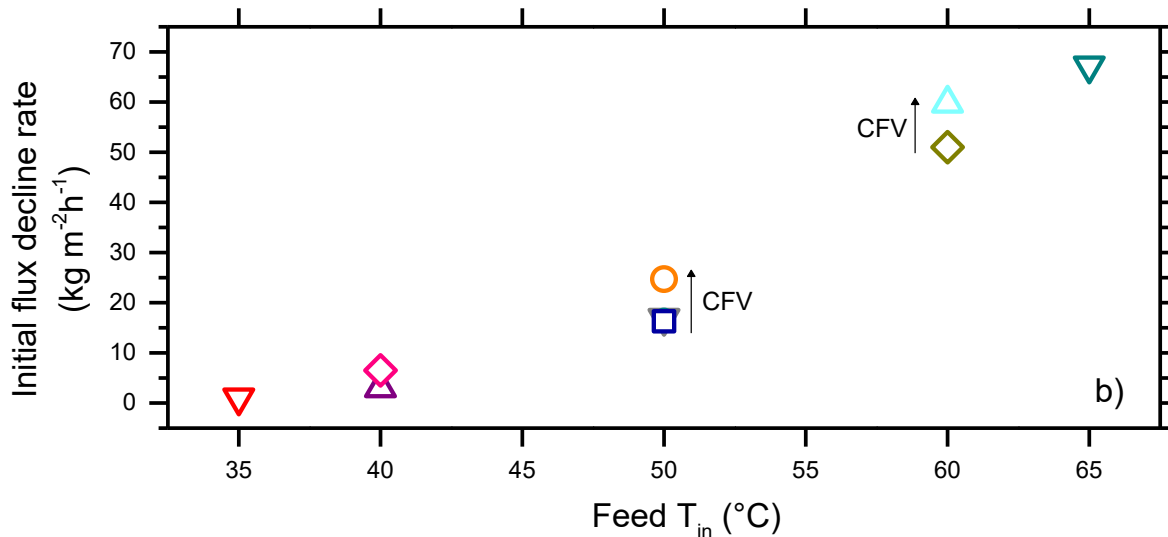
207 **Figure 1.** Results of fouling experiments performed with the synthetic feed water in the  
 208 presence of 500 mg/L humic acid and 20 mM of calcium chloride at different initial permeate  
 209 flux,  $J_0$ , obtained by changing the applied feed temperature and cross-flow velocity in DCMD.  
 210 Water fluxes ( $J_w$ ) were investigated until a volume concentration factor (VCF) of 2.5 was  
 211 reached, at which a value of near-stable final flux was observed for all the experiments. Dash  
 212 lines represent the best linear fit of the first 1.25 volume concentration factor (VCF) of the initial  
 213 flux decline.

214

215 In all the tests, the water flux decreased almost linearly in the initial phase, to then reach an  
 216 approximate flux stabilization over time when the nominal driving force was counterbalanced by  
 217 resistances due to fouling accumulation to yield a constant effective driving force [38]. As  
 218 fouling deposition is proportional to the water transport across the membrane, high accumulation  
 219 typically occurs in the initial phases of operation, contributing to the formation of a cake layer  
 220 during this initial stage [39, 40]. The initial flux decline rates were estimated from the best linear

221 fit (see dash lines in Fig 1a) of the water flux measured between 1 and 1.25 VCF. The values are  
 222 reported as a function of the initial flux  $J_0$  (Fig 2a) and of the inlet feed temperature (Fig 2b). The  
 223 results suggest a smooth and gradually incrementing correlation of the initial flux decline when  
 224 increasing  $J_0$ . The proportional effect of  $J_0$  on the initial flux decline has been also widely  
 225 investigated in osmotically and pressure-driven membrane processes [41-43]. As expected, an  
 226 analogous behavior was observed when looking at the data as a function of the inlet feed  
 227 temperature (Fig 2b), as the driving force is closely related to this parameter. The data also allow  
 228 assessment of the role of the cross-flow velocity, whose increment seems to slightly affect the  
 229 initial flux decline, as an indirect effect of slightly larger values of  $J_0$  observed when increasing  
 230 CFV. The values of near stable flux at the end of the tests,  $J_w$ , and the ratio  $J_w / J_0$  were also  
 231 extrapolated from the flux decline data for each tested condition.





232 **Figure 2.** Plot of the initial flux decline rate as a function of (a) the initial permeate flux  $J_0$ , and  
 233 (b) the inlet feed temperature ( $T_f$ ). The arrows indicate the increment of the cross-flow velocity  
 234 (CFV). Data were extrapolated from dash lines rates reported in Fig 1.

235

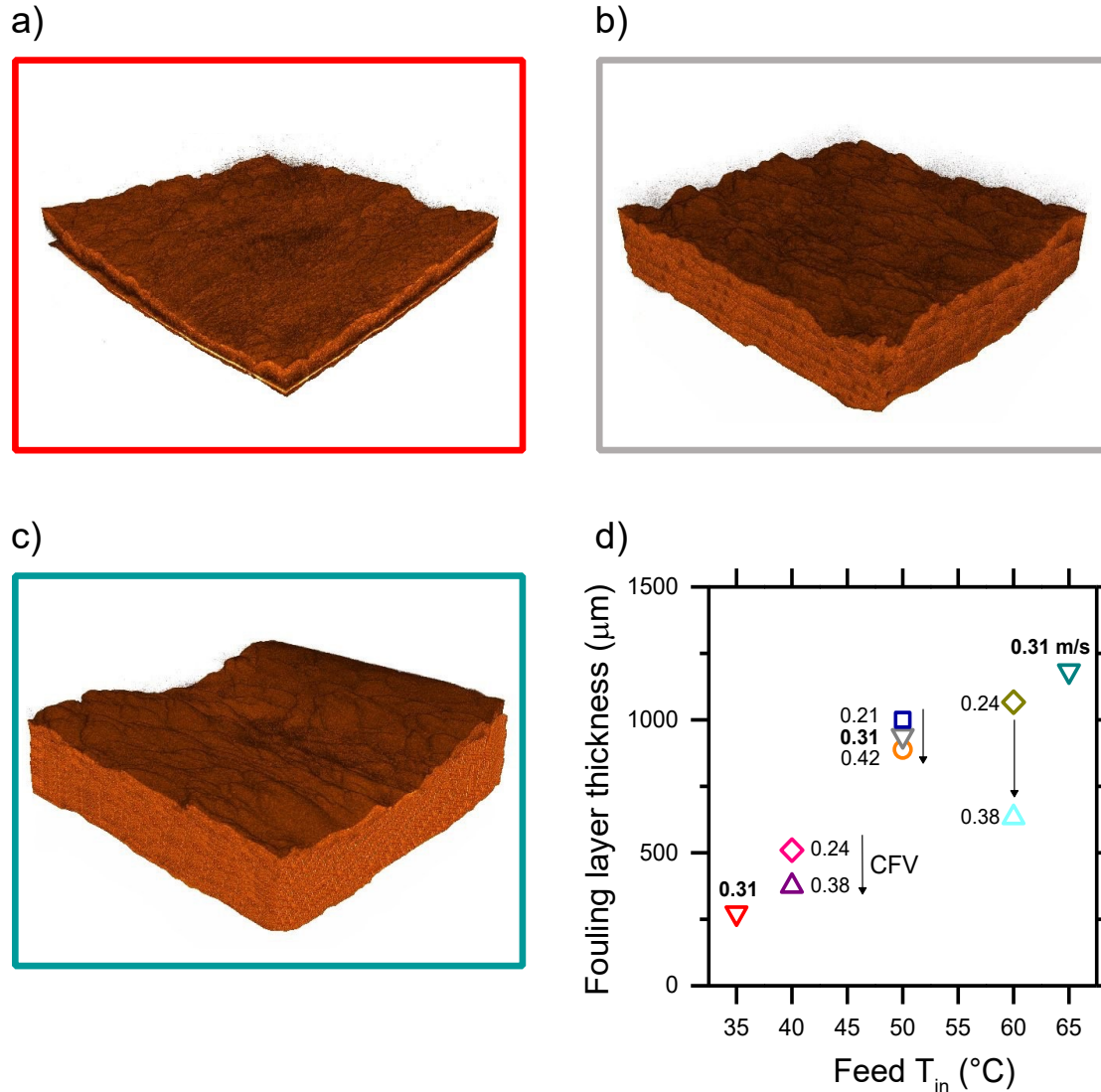
236 A few interesting observations may be made by analyzing the data presented in Figs 1, 2. While  
 237 utilizing an inlet feed temperature set at 65 °C produced an initial flux (22.5 kg m<sup>-2</sup>h<sup>-1</sup>) that is  
 238 nine times higher the flux observed with a temperature equal to 35 °C (2.5 kg m<sup>-2</sup>h<sup>-1</sup>), the flux at  
 239 the end of the tests ( $J_w$ ) was only 3 times larger, reaching roughly 7.5 kg m<sup>-2</sup>h<sup>-1</sup> for the former  
 240 condition, whereas no significant decline in flux was observed at the lower feed temperature.  
 241 These results give reasons for operating at low-medium feed temperatures, namely, at or below  
 242 50 °C for water streams with high fouling potential and if membrane cleanings are not frequently  
 243 operated. In such cases, the long-term productivity may be similar within a wide range of bulk  
 244 feed temperature and working at lower temperature would result in savings in terms of energy  
 245 demand. This may in turn translate, e.g., into cheaper solar fields with smaller footprints if the

246 energy is harvested from the sun, or anyway into a higher energy efficiency and gain output  
247 ration (GOR) value for the overall process.

### 248 **3.1.2 OCT results for the fouling layer thickness**

249 Water flux data were linked to non-invasive direct fouling characterization performed with OCT  
250 to characterize the fouling layer developed on the membrane surface by scanning the central  
251 positions of the cell. Please note that the homogeneity of the fouling layer along the membrane  
252 length was confirmed by preliminarily evaluating the thickness growth at different positions of  
253 the cell. As no spatial gradient was observed, the middle position was selected as a representative  
254 location. The 3D OCT rendering images (Fig 3) show the fouling deposition obtained at  $T_f$  of 35,  
255 50, 65 °C, thus covering the whole range of  $T_f$  investigated. The results highlight the increase of  
256 the foulant deposition by incrementing the inlet feed temperature. In these three examples, the  
257 same cross-flow velocity of 0.31 m/s was applied, representing the central point suggested by  
258 Design Expert within the explored CFV range (see Table S.1). In general, a slight increment of  
259 the foulant roughness was observed by increasing  $T_f$ , as nodule-like and valley-like structures  
260 became more pronounced. This phenomenon was also discussed by Laqbaqbi et al. when testing  
261 DCMD fouling at a temperature close to 70 °C [44].

262



263 **Figure 3.** 3D OCT rendered scans (4mm × 4mm) of the final steady-state foulant layer thickness  
 264 from the experiments conducted at cross-flow velocity of 0.31 m/s and feed inlet temperature of  
 265 35 °C, 50 °C, 65 °C in (a), (b), (c), respectively. The frame color of the OCT images corresponds  
 266 to the color of the associated data points reported in (d). Here, the final thickness is plotted  
 267 against the feed inlet temperature for all the tests. The number indicated close to each data point  
 268 represents the cross-flow velocity associated with the respective test and expressed in m/s.

269

270 For all the experiments, fouling layer thickness measured with the OCT after 2.5 of volume  
271 concentration factor (VCF) is reported in Fig. 3d. In general, a near-linear increment of the  
272 thickness was observed as a function of  $T_f$ , for the entire investigated range of temperatures.  
273 Thus, the thickest deposition was observed for the experiment performed at 65 °C, achieving a  
274 layer thickness of almost 1200  $\mu\text{m}$  at the end of the test. A much smaller layer of roughly 200  
275  $\mu\text{m}$  was observed with  $T_f$  of 35 °C. This last result is in agreement with previous DCMD studies  
276 reporting negligible organic fouling with a feed temperature below 40 °C [45]. As opposed to the  
277 effect of  $T_f$ , higher CFV values were beneficial for reducing the fouling layer development in  
278 MD. The arrows in Fig 3d indicate data points associated with different CFV values. As reported  
279 in the literature, the increment of the shear stress thwarted foulant accumulation by lowering the  
280 boundary layer thickness [46, 47].

281 The results presented imply a strong cause-consequence relation between the operating  
282 parameters in MD and fouling development, but without considering how fouling deposition can  
283 affect the overall driving force, i.e., the thermal balance during the process. Although the  
284 reciprocal influence between the driving force and fouling deposition has been widely  
285 investigated for pressure-driven and osmotically-driven processes [43, 48, 49], further research  
286 efforts are required to evaluate the interaction between governing factors and fouling in MD. In  
287 summary, the *in-situ* observation performed in this study confirmed the link between feed  
288 temperature and fouling propensity. The fouling thickness was found to (i) increase with feed  
289 inlet temperatures  $T_f$ , while (ii) slightly decreasing with cross-flow velocity. The thickness of the  
290 fouling layer may thus also be used as a robust response parameter for the RSM analysis  
291 discussed below.

292

293 **3.2 Modeling of organic fouling in DCMD through response surface methodology (RSM)**  
294

295 **3.2.1 Significance of operating parameters**

296 Organic fouling in DCMD was investigated under different feed inlet temperatures and cross-  
297 flow velocities by performing nine DCMD filtration experiments, with combinations of  
298 operating parameters suggested by the central composite design approach. Based on the results  
299 described above, four parameters were selected as potentially valuable responses for the response  
300 surface analysis: (i) initial flux decline rate, (ii)  $J_w / J_0$  value at the end of the test indicating the  
301 relative loss of productivity due to fouling, (iii) near-stable flux, (iv) final foulant layer thickness.  
302 Experimental results for these parameters were used as input data (responses) to generate the  
303 relative model function. According to Design Expert, all these responses were statistically  
304 significant to both  $T_f$  and CFV, i.e., low p-value. Table 3 summarizes the p-values obtained from  
305 ANOVA. Specifically,  $T_f$  was found to be considerably more significant than CFV. Each  
306 response was fitted by a different model function. The initial flux decline was described by a  
307 quadratic model while all the other responses were adequately described by a linear model, as  
308 can be seen by the absence of cross-correlation terms in Table 3. Within the three linear  
309 responses, CFV was not highly significant, as the p-value was  $> 0.1$ . However, CFV was  
310 included in the model to respect the hierarchy of the statistical method and to improve the fit  
311 [50]. For each response, the final equation calculated by Design Expert and relating operating  
312 parameters with fouling outcomes (responses) is reported in the Supplementary Material  
313 appendix (see Table S.2.).

314 **Table 3** Summary of response significance values estimated by ANOVA statistical analysis.

Source	Initial flux decline p-value	Final $J_w/J_0$ p-value	Final flux p-value	Final thickness p-value
--------	---------------------------------	----------------------------	-----------------------	----------------------------

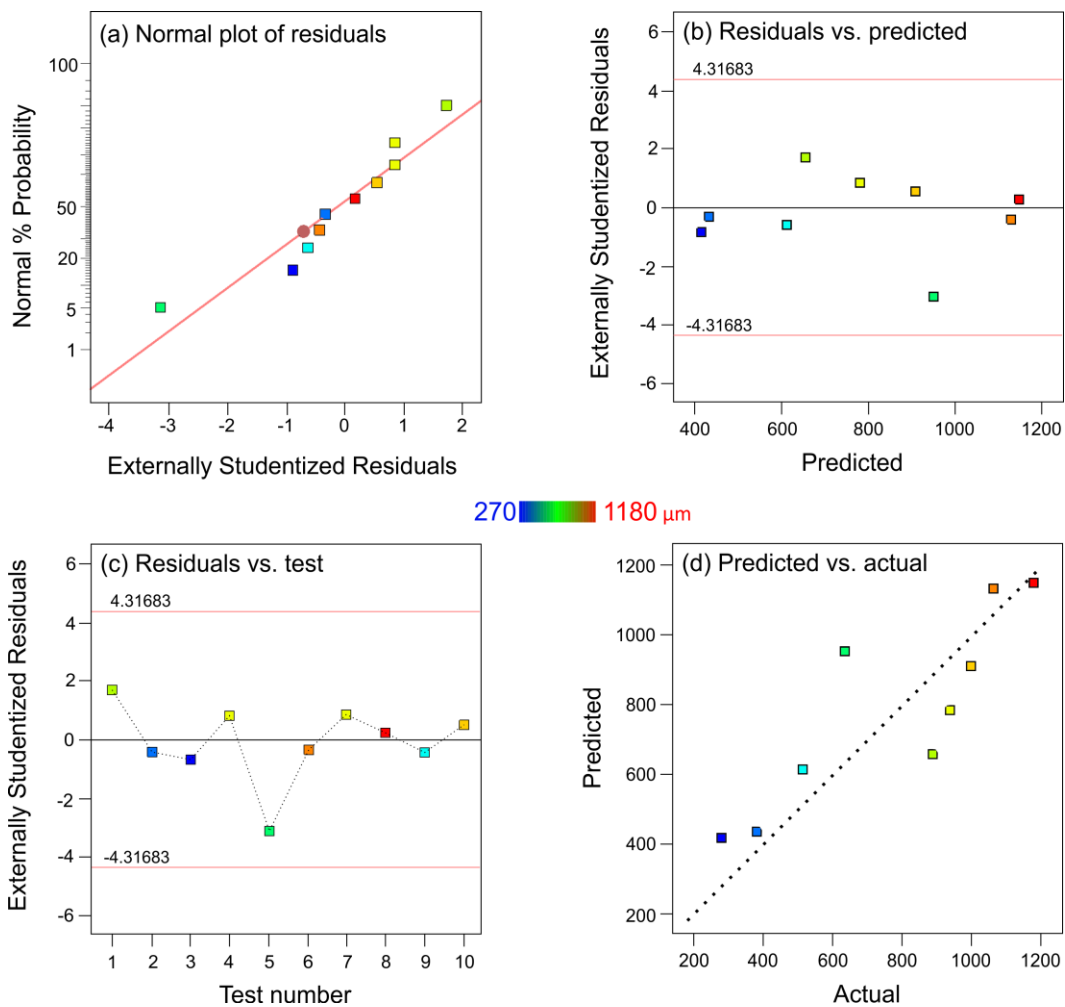
<b>Model</b>	0.0001	0.0004	< 0.0001	0.0133
A-Cross-flow velocity	0.0835	0.4156	0.2145	0.2191
B-Feed temperature	< 0.0001	0.0001	< 0.0001	0.0059
AB	0.0812			
A <sup>2</sup>	0.1153			
B <sup>2</sup>	0.0017			

315

316 To provide a detailed statistical analysis, the diagnostic plots of the initial flux decline, the final  
317 flux, and the final  $J_w/J_0$  values are shown in Fig S.2, S.3 and S.4, respectively. Figure 4 displays  
318 the diagnostic plots for the final foulant layer thickness. Please note that the following discussion  
319 relates directly to layer thickness, but the conclusions and implications are also valid for the  
320 other selected responses. Figure 4a reports the normal probability plot of residuals (error terms),  
321 a graphical tool for comparing a data set with the normal distribution: if the data can be  
322 adequately described with a normal distribution, characterized by a mean and a variance, then a  
323 plot of the theoretical percentiles of the normal distribution versus the observed sample  
324 percentiles should be approximately linear. In Fig 4a, the red linear line represents the theoretical  
325 normal distribution while the ten dots represent the observed samples (10 runs, Table S1). For all  
326 the responses, normal probability plot of the residuals fell on a straight line, which implies that  
327 error terms had a normal distribution [51, 52].

328 Figure 4b shows that all points are scattered around the 0 y-axis (variance or standard deviation)  
329 reflecting equal or similar variances of collected data. In fact, nine points out of ten lie within  
330 two standard deviations, meaning that 95% of values are included in this range (empirical rule).  
331 In this case, the variance of residuals can be considered as a constant (homoscedasticity).  
332 Homoscedasticity is an important assumption of parametric statistical tests. In Fig. 4c, residuals  
333 vs. data points do not follow a specific pattern, which suggests that responses are not dependent  
334 on the order of runs. Lastly, Fig. 4d illustrates that predicted values vs. experimental values lay

335 on a straight 45 degree line, an indication of high-quality modeling outcome. In conclusion, the  
 336 diagnostic plots of all the responses indicate the robustness of the statistical analysis, which  
 337 enable to assess the impact of the operating parameters on the organic fouling behavior in MD.

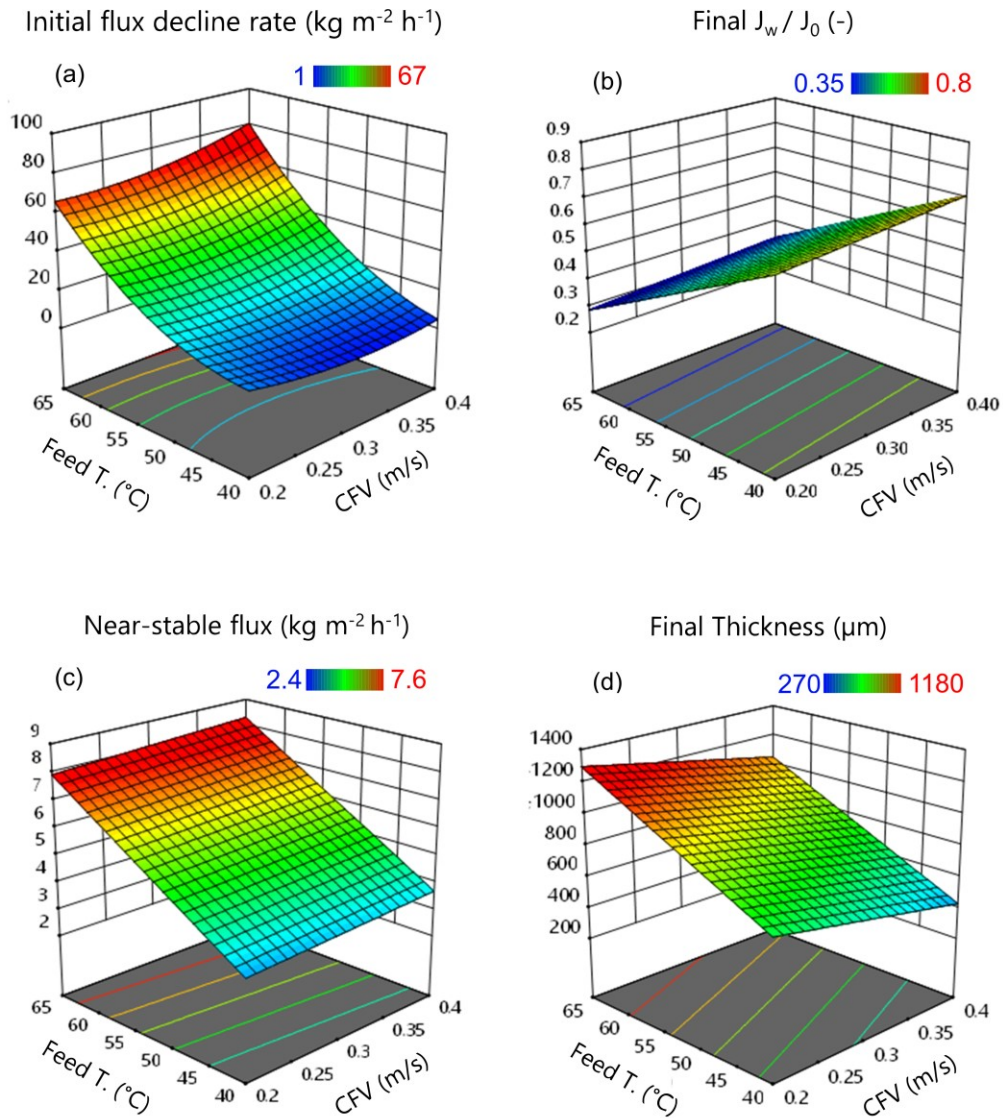


338  
 339 **Figure 4.** Diagnostic plots for the foulant layer thickness response: (a) normal % probability vs.  
 340 residuals; (b) residuals vs. predicted; (c) residuals vs. run order; (d) predicted vs. actual.

341

### 342 3.2.2 Single responses evaluation

343 Fig 5 shows the outcome of the RSM model in terms of effects of operating parameters, i.e.,  
344 temperature and cross-flow velocity, on the fouling behavior, namely, initial flux decline rate,  
345 final  $J_w/J_0$ , the near-stable flux, and the final layer thickness. This discussion aims at providing  
346 an effective view of fouling behavior in the whole range of investigated conditions of  $T_f$  and  
347 CFV and to facilitate any direct comparison among the selected fouling parameters. In  
348 accordance with the description in the section above, all the responses were mainly governed by  
349 the feed temperature. Specifically, Fig 5b shows how contour values decrease from a  $J_w / J_0$  of  
350 0.7 to below 0.3 when the  $T_f$  increases from 40 to 65 °C, thus only roughly  $1 \text{ kg m}^{-2}\text{h}^{-1}$  of stable  
351 flux is gained for each 5 °C-step in  $\Delta T_f$  (see Fig 5c). As illustrated in Fig 5c, a net increment of  
352 the fouling deposition can be observed by increasing  $T_f$ , as a twofold increase of layer thickness  
353 is associated to an increase of the temperature from 40 to 65 °C.



354

355 **Figure 5.** 2D surface response plots as a function of the feed inlet temperature and cross-flow  
 356 velocity for the (a) initial flux decline rate, (b) final to initial flux ration, (c) near-stable flux, and  
 357 (d) final foulant layer thickness. The near-stable flux is the flux at volume concentration factor of  
 358 2.5 for the experiments reported in Fig 1. The magnitude for each response increases from blue  
 359 to red and is also indicated by numeric values for each contour line.

360

361 In contrast to feed inlet temperature, different behaviors were observed by varying the cross-flow  
362 velocity. The initial flux decline rate was more affected by the CFV at higher  $T_f$  values (see Fig  
363 5a). This result can be explained by the proportionality between  $T_f$  and temperature polarization  
364 (TP) [52]. Faster CFVs thwart TP and this effect is more pronounced when TP tends to be of  
365 greater magnitude, that is, at higher values of  $T_f$ . This translates into larger  $J_0$  (see Fig 1) and the  
366 ensuing steeper flux decline, as observed for CFV values above 0.3 m/s [53, 54]. On the other  
367 hand, increasing CFV yielded a positive outcome in terms of productivity when considering the  
368 magnitude of the near-stable flux (see Fig 5b, c), likely due to lower fouling deposition  
369 associated with smaller boundary layers, as observed in Fig 5c. In fact, the OCT scans  
370 highlighted a reduction in fouling layer thickness by increasing the CFV. Interestingly, the CFV  
371 was more impactful in decreasing the foulant thickness rather than increasing the overall flux  
372 decline  $J_w / J_0$ , implying that foulant thickness and flux loss are not directly correlated but that a  
373 complex mechanism is in play. This result might be rationalized with the fact that these two  
374 parameters are not independent, for example,  $J_w$  may not simply intensify the likelihood of  
375 foulant deposition but simultaneously cause enhanced compactness of the resulting layer [55].  
376 Both thickness and compactness of the foulant layer play a role in mass and heat transport, and  
377 thicker but more porous layer may be less detrimental than thin dense layers that would produce  
378 a larger variation in diffusion coefficients and thermal conductivity with respect to the bulk  
379 solution.

380 In conclusion, the RSM analysis well depicted the link between fouling propensity and feed  
381 temperature, as fouling behavior worsened with the increase of the feed inlet temperature,  
382 thereby negatively affecting the flux decline,  $J_w/J_0$ , while a positive but gradually more marginal  
383 enhancement of productivity (near-stable flux) was observed when increasing the feed inlet

384 temperature. Moreover, it was found that the increase in cross-flow velocity led to a slight  
385 decrease of the fouling thickness deposited on the membrane, while keeping an overall benefit in  
386 terms of productivity.

## 387 **Conclusions**

388 Organic fouling in MD process was investigated using humic acid and calcium chloride in  
389 the feed solution. The goal of this study was to assess the role of the feed temperature and  
390 cross-flow velocity on fouling behaviour in DCMD. The different operating conditions of the  
391 experiments were selected through Design Expert software aiming to build the model  
392 function of the selected responses. The four process performance parameters selected as  
393 responses (dependent variables) for the RSM were: (i) the initial flux decline rate, (ii) the  
394 near-stable flux measured at the end of the tests, (iii) the stable to initial flux ration,  $J_w / J_0$ ,  
395 and (iv) the final fouling layer thickness.

396 Higher influence of feed inlet temperature than cross-flow velocity on loss of productivity was  
397 observed experimentally and then confirmed by robust statistical analysis, due to the major  
398 role of flux in the development of organic fouling in DCMD. In detail, a sharp increment in  
399 the overall flux decline,  $J_w/J_0$  occurred at higher feed inlet temperatures, making the case for  
400 the need to select an appropriately transmembrane temperature difference that guarantees  
401 feasible fluxes but also minimizes loss of driving force and energy demand. The benefits in  
402 water productivity obtained by increasing the feed temperature were always offset by higher  
403 fouling deposition.

404 Another interesting trade-off between more rapid initial flux decline and thinner layer  
405 thickness was observed by increasing cross-flow velocity above 0.3 m/s. Layer thickness is  
406 only one of many aspects of the foulant layer that relates to productivity loss, others may  
407 include density, pore structure and thermal conductivity, which can directly influence mass  
408 and heat transport through this unmixed layer. Optical coherence tomography (OCT) was used  
409 in this study to assess layer thickness, but further efforts are needed to deepen investigations

410 on foulant deposition and on how layer characteristics relate to deposition mode and then  
411 flux loss. Overall, working at relatively high cross-flow velocity may be beneficial at high  
412 values of the nominal driving force, i.e., transmembrane temperature difference, while the  
413 results suggest that the effect of channel feed flow velocity may not play a significant role  
414 when the flux is below a certain level, approximately  $10 \text{ kg m}^{-2}\text{h}^{-1}$ .

415 Finally, the proposed approach is not limited to this application but was proven to be a valuable  
416 tool to assess the role of the process parameters and governing factors on fouling and process  
417 performance in membrane distillation (MD). The results of this study highlight the effectiveness  
418 of combining flux data, OCT characterization, and response surface methodology (RSM) to  
419 advance the understanding of fouling in MD and open future perspective related to this crucial  
420 topic to making MD feasible at commercial scale.

421  
422  
423  
424  
425  
426  
427  
428  
429  
430  
431  
432  
433  
434

***Supplementary material***

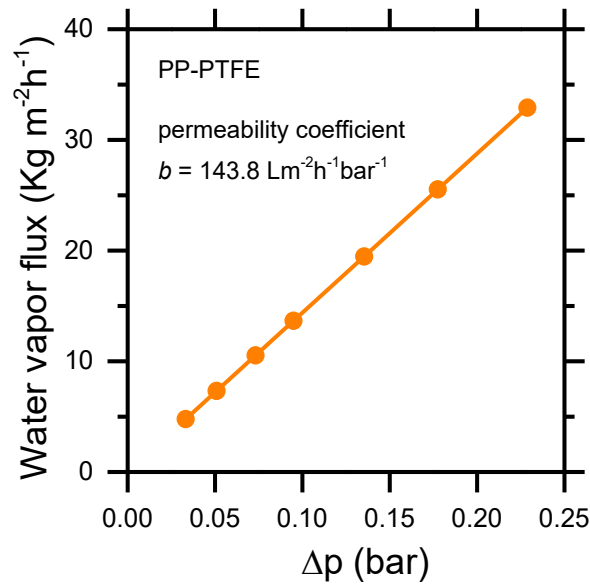
**Assessing the effect of feed temperature and cross-flow velocity on organic fouling in membrane distillation using response surface methodology**

Francesco Ricceri<sup>a</sup>, Bastiaan Blankert<sup>b</sup>, Johannes S. Vrouwenvelder<sup>b</sup>, Alberto Tiraferri<sup>a\*</sup>, Luca Fortunato<sup>b\*</sup>

<sup>a</sup> Department of Environment, Land and Infrastructure Engineering (DIATI), Politecnico di Torino, Corso Duca degli Abruzzi 24, Turin, 10129, Italy

<sup>b</sup> Water Desalination and Reuse Center (WDRC), King Abdullah University of Science and Technology (KAUST), Biological & Environmental Science & Engineering Division (BESE), Thuwal 23955-6900, Saudi Arabia

\* Corresponding authors



435

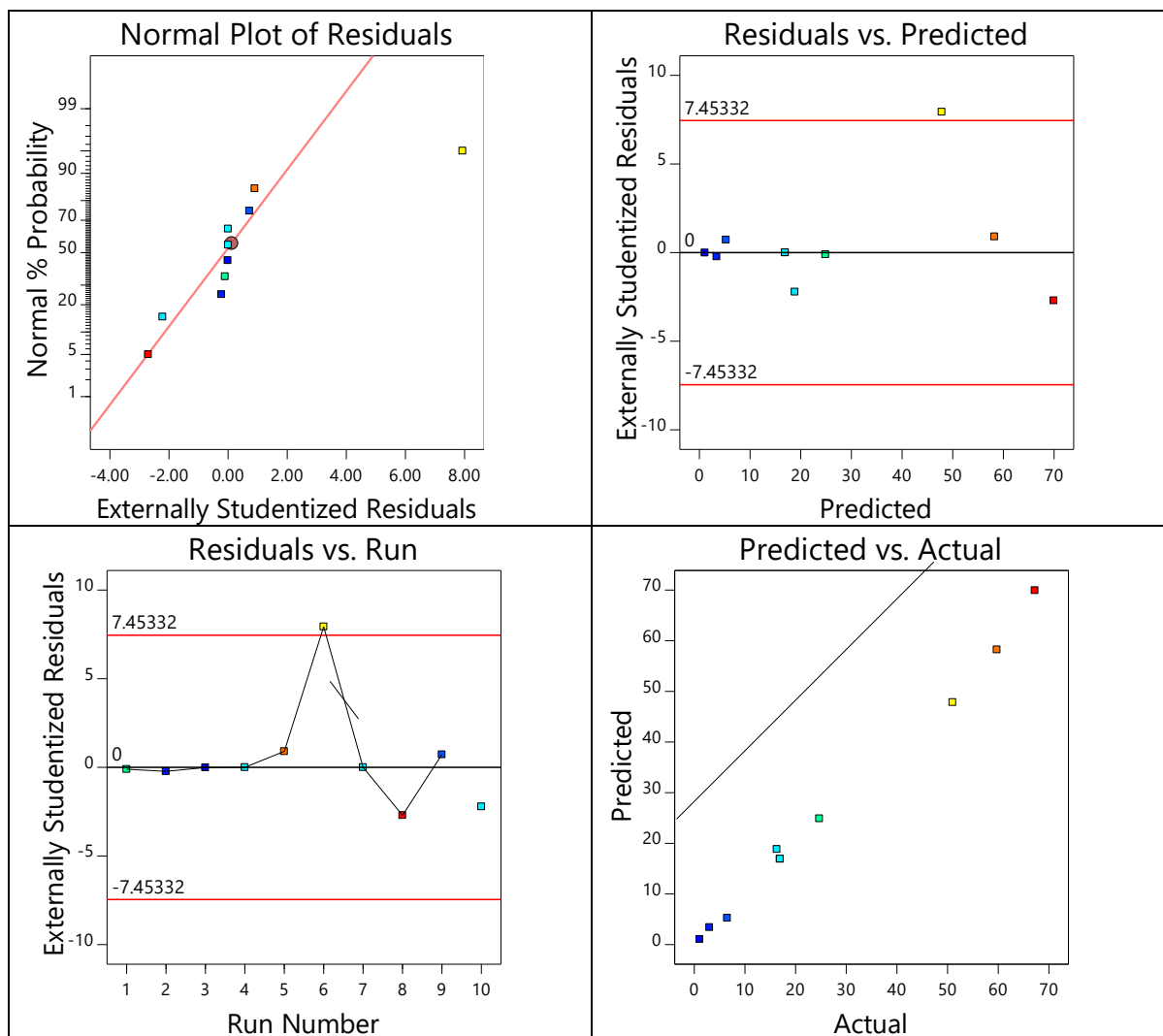
436 **Figure S.1.** Linear correlation between the obtained water vapor flux as a function of the  
 437 applied vapor tension difference for the PP-PTFE membrane. The permeability,  $b$ , is  
 438 reported.

439

440 **Table S.1.** List of the experiments suggested by Design Expert software for different  
 441 combinations of cross-flow velocity and inlet feed temperature. Related experimental results  
 442 for each response are also listed from the third column. C.P indicates the central point, a  
 443 repetition of the 4<sup>th</sup> run, required by the software to retrieve a better model fitting.

Run	CFV	$T_f$	Initial flux decline	Final flux	Final thickness	$J_w/J_0$
-	m/s	°C	$\text{Kg m}^{-2}\text{h}^{-1}/[-]$	$\text{Kg m}^{-2}\text{h}^{-1}$	$\mu\text{m}$	-
1	0.42	50.0	24.7	5.8	888	0.48
2	0.39	39.4	3.0	3.6	375	0.79
3	0.31	35.0	1.1	2.4	273	0.80
4	0.31	50.0	16.9	5.4	940	0.52
5	0.39	60.6	59.7	7.4	633	0.39
6	0.24	60.6	51.0	7.6	1066	0.42
7	0.31	65.0	67.2	7.6	1183	0.34
8	0.24	39.4	6.5	3.2	510	0.64
9	0.21	50.0	16.3	5.2	1000	0.47
C.P	0.31	50.0	17.6	5.1	920	0.57

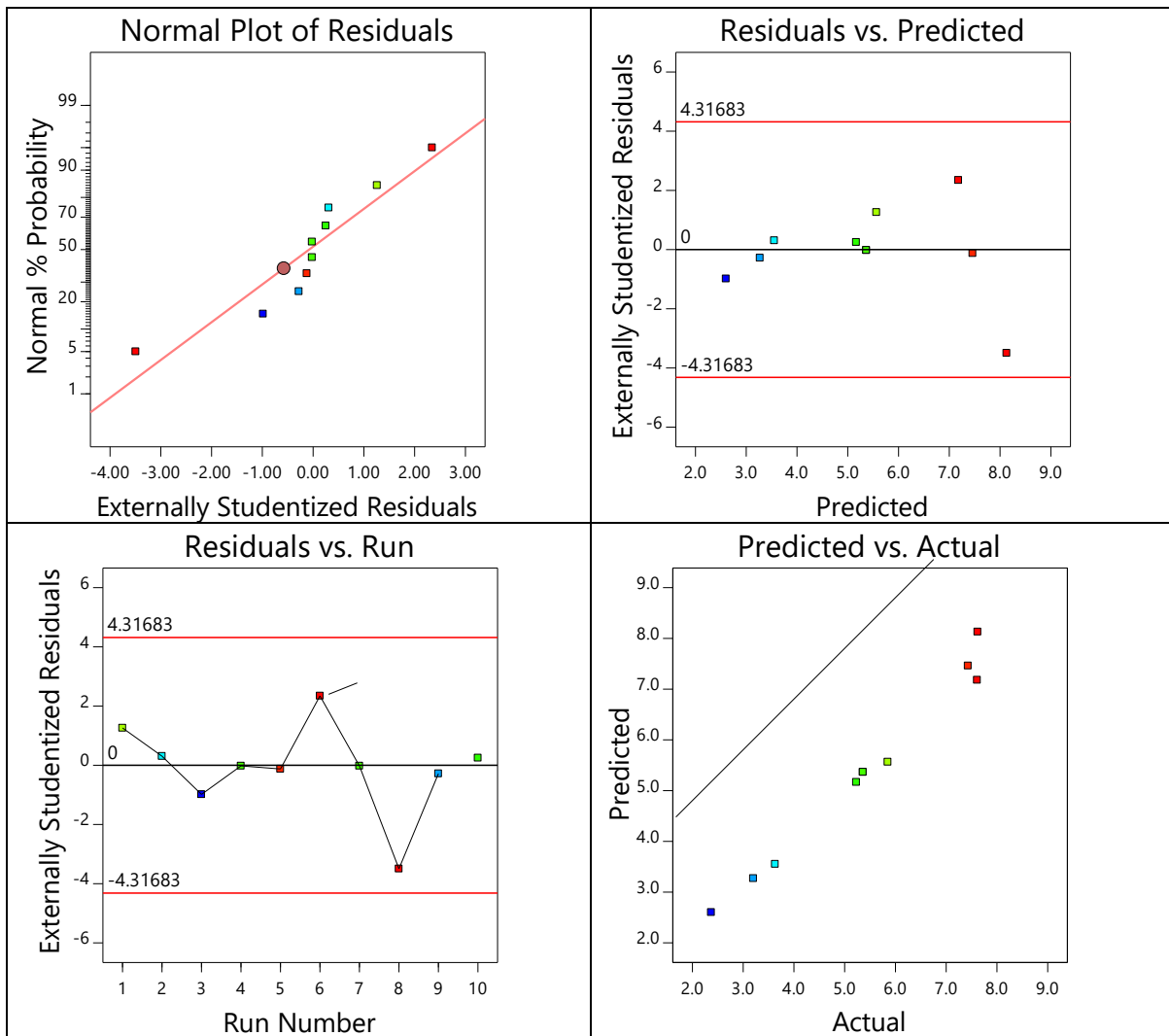
444



446

447 **Figure S.2.** Diagnostic plots for initial flux decline rate as response: (a) normal %  
 448 probability vs. residuals; (b) residuals vs. predicted; (c) residuals vs. run order; (d) predicted  
 449 vs. actual.

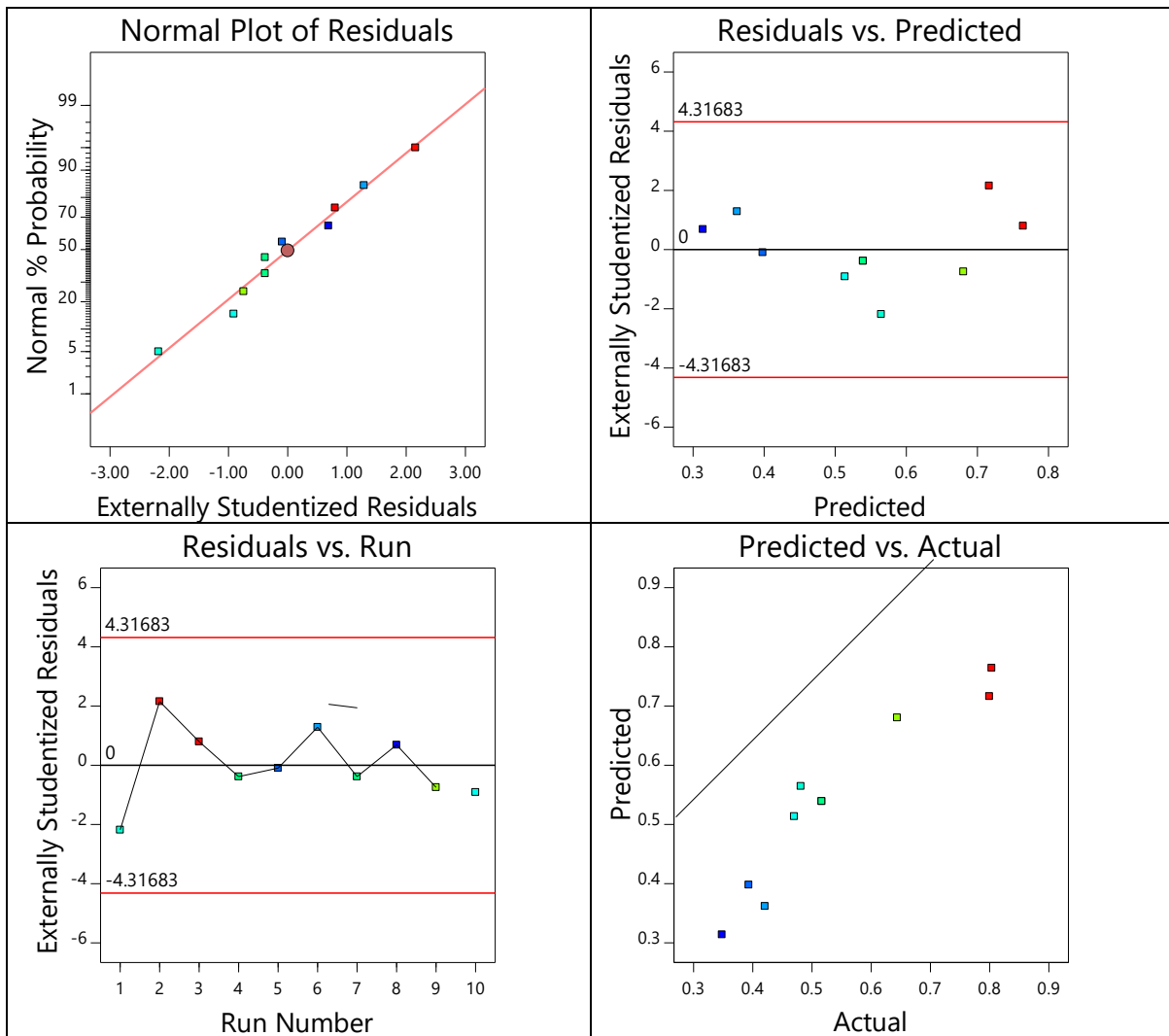
450



451

452 **Figure S.3.** Diagnostic plots for near-stable flux at the end of the test as response: (a) normal  
 453 % probability vs. residuals; (b) residuals vs. predicted; (c) residuals vs. run order; (d)  
 454 predicted vs. actual.

455



456

457 **Figure S.4.** Diagnostic plots for  $J_w/J_0$  as response: (a) normal % probability vs. residuals; (b)  
 458 residuals vs. predicted; (c) residuals vs. run order; (d) predicted vs. actual.

459

460 **Tab S.2.** Final equations computed by the statistical analysis and relating operating  
 461 parameters to fouling behaviour. The equation can be used to make predictions about each  
 462 response.

		Initial Flux decline	Final Flux	Final Thickness	$J_w/J_0$
		+206.19420	+5.37	+780.80	+1.21292
A-Cross flow velocity	*	-452.03539	+0.1409	-90.80	+0.243943
B-Feed temperature	*	-7.19720	+1.95	+262.62	-0.015014
AB	*	+3.90112			

A <sup>2</sup>	*	+453.12607			
B <sup>2</sup>	*	+0.082623			

463

464 **Appendix**

465 The model is generated for the four responses and is based on experimental data collected in  
466 the lab fitting a linear model for the final flux, final thickness, and final  $J_w/J_0$  responses and a  
467 fitting a quadratic model for the initial flux decline rate response. The most general equation  
468 is reported here below:

469 
$$y = \beta_0 + \sum_{k_i = 1} \beta_i x_i + \sum_{k_i = 1} \beta_{ii} x_i^2 + \sum_{k_j = i + 1} \beta_{ij} x_i x_j + \varepsilon$$

470 (Eq S.2)

471 where y is the predicted response, x represents the factors, k is the number of factors,  $\beta_0$  is the  
472 constant coefficient, and  $\beta_i$ ,  $\beta_{ii}$ , and  $\beta_{ij}$  are the regression coefficients of linear, quadratic, and  
473 interaction terms, respectively. To select the amount of experimental data to be collected,  
474 Central Composite Design (CCD) was applied. This design defines 2k corner points, 2k axial  
475 points, where k is the number of independent variables (or factors) selected, and a central  
476 point. In this study, two factors (Feed inlet temperature and feed cross-flow velocity) were  
477 selected. The number of experiments was directly calculated by the software according to the  
478 equation  $n = 2^k \cdot 2k + Cp$ , resulting in a total of 10 experiments, one of them represented by  
479 the central point (Cp). These test are a combination of different factors levels defined by the  
480 coded values calculated by applying the formulas in Table S2. The coded value associated  
481 with  $\alpha$  is representative of the rotatability of the model which suggested Practical alpha due to  
482  $k < 6$  and equal to 1,41, which represents the distance.

483

484

**Table S2.** Coded and un-coded values for CCD

Coded value	Un-coded value
$-\alpha$	$X_{min}$
-1	$\frac{(\alpha - 1)X_{max} + (\alpha + 1)X_{min}}{2\alpha}$
0	$\frac{X_{max} + X_{min}}{2}$
+1	$\frac{(\alpha - 1)X_{min} + (\alpha + 1)X_{max}}{2\alpha}$
$+\alpha$	$X_{max}$

485

- 487 [1] N. Thomas, M.O. Mavukkandy, S. Loutatidou, H.A. Arafat, Membrane distillation research &  
488 implementation: Lessons from the past five decades, *Separation and Purification Technology*, 189  
489 (2017) 108-127.
- 490 [2] L.M. Camacho, L. Dumée, J. Zhang, J.-d. Li, M. Duke, J. Gomez, S. Gray, Advances in membrane  
491 distillation for water desalination and purification applications, *Water*, 5 (2013) 94-196.
- 492 [3] I. Hitsov, L. Eykens, W. De Schepper, K. De Sitter, C. Dotremont, I. Nopens, Full-scale direct  
493 contact membrane distillation (DCMD) model including membrane compaction effects, *Journal of*  
494 *membrane science*, 524 (2017) 245-256.
- 495 [4] G. Dong, J.F. Kim, J.H. Kim, E. Drioli, Y.M. Lee, Open-source predictive simulators for scale-up of  
496 direct contact membrane distillation modules for seawater desalination, *Desalination*, 402 (2017)  
497 72-87.
- 498 [5] H. Susanto, Towards practical implementations of membrane distillation, *Chemical Engineering*  
499 *and Processing: Process Intensification*, 50 (2011) 139-150.
- 500 [6] M. Khayet, T. Matsuura, *Membrane distillation: principles and applications*, (2011).
- 501 [7] B. Ashoor, S. Mansour, A. Giwa, V. Dufour, S. Hasan, Principles and applications of direct contact  
502 membrane distillation (DCMD): a comprehensive review, *Desalination*, 398 (2016) 222-246.
- 503 [8] T. Horseman, Y. Yin, K.S. Christie, Z. Wang, T. Tong, S. Lin, Wetting, scaling, and fouling in  
504 membrane distillation: State-of-the-art insights on fundamental mechanisms and mitigation  
505 strategies, *ACS ES&T Engineering*, 1 (2020) 117-140.
- 506 [9] M. Rezaei, D.M. Warsinger, M.C. Duke, T. Matsuura, W.M. Samhaber, Wetting phenomena in  
507 membrane distillation: Mechanisms, reversal, and prevention, *Water research*, 139 (2018) 329-352.
- 508 [10] E. Guillen-Burrieza, M. Mavukkandy, M. Bilad, H. Arafat, Understanding wetting phenomena in  
509 membrane distillation and how operational parameters can affect it, *Journal of Membrane Science*,  
510 515 (2016) 163-174.
- 511 [11] S. Shao, D. Shi, J. Hu, W. Qing, X. Li, X. Li, B. Ji, Z. Yang, H. Guo, C.Y. Tang, Unraveling the Kinetics  
512 and Mechanism of Surfactant-Induced Wetting in Membrane Distillation: An In Situ Observation with  
513 Optical Coherence Tomography, *Environmental science & technology*, (2021).
- 514 [12] D. Hou, Z. Yuan, M. Tang, K. Wang, J. Wang, Effect and mechanism of an anionic surfactant on  
515 membrane performance during direct contact membrane distillation, *Journal of Membrane Science*,  
516 595 (2020) 117495.
- 517 [13] K.S. Christie, Y. Yin, S. Lin, T. Tong, Distinct behaviors between gypsum and silica scaling in  
518 membrane distillation, *Environmental science & technology*, 54 (2019) 568-576.
- 519 [14] M. Gryta, Fouling in direct contact membrane distillation process, *Journal of membrane science*,  
520 325 (2008) 383-394.
- 521 [15] P. Wang, T.-S. Chung, Recent advances in membrane distillation processes: Membrane  
522 development, configuration design and application exploring, *Journal of membrane science*, 474  
523 (2015) 39-56.
- 524 [16] F. Ricceri, M. Giagnorio, G. Farinelli, G. Blandini, M. Minella, D. Vione, A. Tiraferri, Desalination  
525 of produced Water by Membrane Distillation: Effect of the feed components and of a pre-treatment  
526 by fenton oxidation, *Scientific reports*, 9 (2019) 1-12.
- 527 [17] L. Fortunato, H. Elcik, B. Blankert, N. Ghaffour, J. Vrouwenvelder, Textile dye wastewater  
528 treatment by direct contact membrane distillation: Membrane performance and detailed fouling  
529 analysis, *Journal of Membrane Science*, 636 (2021) 119552.
- 530 [18] J. Guo, L. Fortunato, B.J. Deka, S. Jeong, A.K. An, Elucidating the fouling mechanism in  
531 pharmaceutical wastewater treatment by membrane distillation, *Desalination*, 475 (2020) 114148.
- 532 [19] J.-G. Lee, Y. Jang, L. Fortunato, S. Jeong, S. Lee, T. Leiknes, N. Ghaffour, An advanced online  
533 monitoring approach to study the scaling behavior in direct contact membrane distillation, *Journal of*  
534 *Membrane Science*, 546 (2018) 50-60.

535 [20] A. Abdel-Karim, S. Leaper, C. Skuse, G. Zaragoza, M. Gryta, P. Gorgojo, Membrane cleaning and  
536 pretreatments in membrane distillation-a review, *Chemical Engineering Journal*, (2021) 129696.

537 [21] C.A. Robbins, Y. Yin, A.J. Hanson, J. Blotevogel, T. Borch, T. Tong, Mitigating membrane wetting  
538 in the treatment of unconventional oil and gas wastewater by membrane distillation: A comparison  
539 of pretreatment with omniphobic membrane, *Journal of Membrane Science*, (2021) 120198.

540 [22] G. Naidu, S. Jeong, S.-J. Kim, I.S. Kim, S. Vigneswaran, Organic fouling behavior in direct contact  
541 membrane distillation, *Desalination*, 347 (2014) 230-239.

542 [23] F. Wendland, A. Blum, M. Coetsiers, R. Gorova, J. Griffioen, J. Grima, K. Hinsby, R. Kunkel, A.  
543 Marandi, T. Melo, European aquifer typology: a practical framework for an overview of major  
544 groundwater composition at European scale, *Environmental Geology*, 55 (2008) 77-85.

545 [24] R. Valladares Linares, L. Fortunato, N. Farhat, S. Bucs, M. Staal, E. Fridjonsson, M. Johns, J.S.  
546 Vrouwenvelder, T. Leiknes, Mini-review: novel non-destructive in situ biofilm characterization  
547 techniques in membrane systems, *Desalination and Water Treatment*, 57 (2016) 22894-22901.

548 [25] L. Fortunato, A.F. Lamprea, T. Leiknes, Evaluation of membrane fouling mitigation strategies in  
549 an algal membrane photobioreactor (AMPBR) treating secondary wastewater effluent, *Science of  
550 The Total Environment*, 708 (2020) 134548.

551 [26] L. Fortunato, Y. Jang, J.-G. Lee, S. Jeong, S. Lee, T. Leiknes, N. Ghaffour, Fouling development in  
552 direct contact membrane distillation: Non-invasive monitoring and destructive analysis, *Water  
553 research*, 132 (2018) 34-41.

554 [27] F. Ricceri, G. Farinelli, M. Giagnorio, A. Zamboi, A. Tiraferri, Optimization of physico-chemical  
555 and membrane filtration processes to remove high molecular weight polymers from produced water  
556 in enhanced oil recovery operations, *Journal of Environmental Management*, 302 (2022) 114015.

557 [28] I. Righetto, R.A. Al-Juboori, J.U. Kaljunen, A. Mikola, Multipurpose treatment of landfill leachate  
558 using natural coagulants—Pretreatment for nutrient recovery and removal of heavy metals and  
559 micropollutants, *Journal of Environmental Chemical Engineering*, 9 (2021) 105213.

560 [29] I. Righetto, R.A. Al-Juboori, J.U. Kaljunen, A. Mikola, Wastewater treatment with starch-based  
561 coagulants for nutrient recovery purposes: Testing on lab and pilot scales, *Journal of Environmental  
562 Management*, 284 (2021) 112021.

563 [30] M. Ahmadi, F. Vahabzadeh, B. Bonakdarpour, E. Mofarrah, M. Mehranian, Application of the  
564 central composite design and response surface methodology to the advanced treatment of olive oil  
565 processing wastewater using Fenton's peroxidation, *Journal of Hazardous Materials*, 123 (2005) 187-  
566 195.

567 [31] T. Rakić, I. Kasagić-Vujanović, M. Jovanović, B. Jančić-Stojanović, D. Ivanović, Comparison of full  
568 factorial design, central composite design, and box-behnken design in chromatographic method  
569 development for the determination of fluconazole and its impurities, *Analytical Letters*, 47 (2014)  
570 1334-1347.

571 [32] M. Shokrollahi, M. Rezakazemi, M. Younas, Producing water from saline streams using  
572 membrane distillation: modeling and optimization using CFD and design expert, *International Journal  
573 of Energy Research*, 44 (2020) 8841-8853.

574 [33] S. Srisurichan, R. Jiraratananon, A. Fane, Humic acid fouling in the membrane distillation  
575 process, *Desalination*, 174 (2005) 63-72.

576 [34] G. Naidu, S. Jeong, S. Vigneswaran, Influence of feed/permeate velocity on scaling development  
577 in a direct contact membrane distillation, *Separation and Purification Technology*, 125 (2014) 291-  
578 300.

579 [35] S. Al-Obaidani, E. Curcio, F. Macedonio, G. Di Profio, H. Al-Hinai, E. Drioli, Potential of membrane  
580 distillation in seawater desalination: thermal efficiency, sensitivity study and cost estimation, *Journal  
581 of membrane science*, 323 (2008) 85-98.

582 [36] F.A. Banat, J. Simandl, Theoretical and experimental study in membrane distillation,  
583 *Desalination*, 95 (1994) 39-52.

584 [37] G.W. Thomson, The Antoine equation for vapor-pressure data, *Chemical reviews*, 38 (1946) 1-  
585 39.

586 [38] C. Boo, S. Hong, M. Elimelech, Relating organic fouling in membrane distillation to  
587 intermolecular adhesion forces and interfacial surface energies, *Environmental science &*  
588 *technology*, 52 (2018) 14198-14207.

589 [39] A. Alkhatib, M.A. Ayari, A.H. Hawari, Fouling mitigation strategies for different foulants in  
590 membrane distillation, *Chemical Engineering and Processing-Process Intensification*, 167 (2021)  
591 108517.

592 [40] A. Hausmann, P. Sancio, T. Vasiljevic, M. Weeks, K. Schroën, S. Gray, M. Duke, Fouling  
593 mechanisms of dairy streams during membrane distillation, *Journal of Membrane Science*, 441  
594 (2013) 102-111.

595 [41] R.W. Field, G.K. Pearce, Critical, sustainable and threshold fluxes for membrane filtration with  
596 water industry applications, *Advances in colloid and interface science*, 164 (2011) 38-44.

597 [42] T.-T. Nguyen, C. Lee, R.W. Field, I.S. Kim, Insight into organic fouling behavior in polyamide thin-  
598 film composite forward osmosis membrane: Critical flux and its impact on the economics of water  
599 reclamation, *Journal of Membrane Science*, 606 (2020) 118118.

600 [43] F. Ricceri, M. Giagnorio, K.R. Zodrow, A. Tiraferri, Organic fouling in forward osmosis: Governing  
601 factors and a direct comparison with membrane filtration driven by hydraulic pressure, *Journal of*  
602 *Membrane Science*, 619 (2021) 118759.

603 [44] M. Laqbaqbi, M. García-Payo, M. Khayet, J. El Kharraz, M. Chaouch, Application of direct contact  
604 membrane distillation for textile wastewater treatment and fouling study, *Separation and*  
605 *Purification Technology*, 209 (2019) 815-825.

606 [45] J. Ortiz de Zárate, C. Rincón, J. Mengual, Concentration of bovine serum albumin aqueous  
607 solutions by membrane distillation, *Separation science and technology*, 33 (1998) 283-296.

608 [46] S. Srisurichan, R. Jiratananon, A. Fane, Mass transfer mechanisms and transport resistances in  
609 direct contact membrane distillation process, *Journal of membrane science*, 277 (2006) 186-194.

610 [47] L. Eykens, I. Hitsov, K. De Sitter, C. Dotremont, L. Pinoy, I. Nopens, B. Van der Bruggen, Influence  
611 of membrane thickness and process conditions on direct contact membrane distillation at different  
612 salinities, *Journal of Membrane Science*, 498 (2016) 353-364.

613 [48] M.S. Toran, A. D'Haese, I. Rodríguez-Roda, W. Gernjak, Fouling propensity of novel TFC  
614 membranes with different osmotic and hydraulic pressure driving forces, *Water Research*, 175  
615 (2020) 115657.

616 [49] F.A. Siddiqui, Q. She, A.G. Fane, R.W. Field, Exploring the differences between forward osmosis  
617 and reverse osmosis fouling, *Journal of Membrane Science*, 565 (2018) 241-253.

618 [50] N. Biglarijoo, S.A. Mirbagheri, M. Ehteshami, S.M. Ghaznavi, Optimization of Fenton process  
619 using response surface methodology and analytic hierarchy process for landfill leachate treatment,  
620 *Process Safety and Environmental Protection*, 104 (2016) 150-160.

621 [51] H. Pashaei, A. Ghaemi, M. Nasiri, B. Karami, Experimental modeling and optimization of CO<sub>2</sub>  
622 absorption into piperazine solutions using RSM-CCD methodology, *ACS omega*, 5 (2020) 8432-8448.

623 [52] M. Qtaishat, T. Matsuura, B. Kruczek, M. Khayet, Heat and mass transfer analysis in direct  
624 contact membrane distillation, *Desalination*, 219 (2008) 272-292.

625 [53] Z. Ding, L. Liu, Z. Liu, R. Ma, Fouling resistance in concentrating TCM extract by direct contact  
626 membrane distillation, *Journal of Membrane Science*, 362 (2010) 317-325.

627 [54] A. Hausmann, P. Sancio, T. Vasiljevic, U. Kulozik, M. Duke, Performance assessment of  
628 membrane distillation for skim milk and whey processing, *Journal of Dairy Science*, 97 (2014) 56-71.

629 [55] M. Laqbaqbi, J.A. Sanmartino, M. Khayet, C. García-Payo, M. Chaouch, Fouling in membrane  
630 distillation, osmotic distillation and osmotic membrane distillation, *Applied Sciences*, 7 (2017) 334.

631